2002-01-01

# An Efficient Procedure for Viscous Propeller Flow Field Calculations

Fergal Boyle
*Technological University Dublin*, fergal.boyle@tudublin.ie



## Recommended Citation

Boyle, F.: An Efficient Procedure for Viscous Propeller Flow Field Calculations. 38th American Institute of Aeronautics and Astronautics/American Society of Mechanical Engineers/Society of Automotive Engineers/American Society for Engineering Education Joint Propulsion Conference. IAA Paper No. 2002-3859. Indianapolis, Indiana, USA, 2002. doi:10.2514/6.2002-3859



Funder: DIT

# AN EFFICIENT PROCEDURE FOR VISCOUS PROPELLER FLOW FIELD CALCULATIONS

**Fergal Boyle***
**Department of Mechanical Engineering**
**Dublin Institute of Technology, Bolton St, Dublin 1, Ireland**

## Abstract

An efficient procedure has been developed for the computation of the three-dimensional, compressible, viscous flow field around a general propeller geometry with the inflow at zero angles of incidence and yaw. The solution procedure combines a recently developed Reynolds-Averaged-Navier-Stokes equations solver with a commercially available grid generator designed specifically for turbomachinery configurations. Preliminary results from the calculation of laminar and turbulent incompressible flow over a flat plate demonstrate that the flow solver is capable of capturing boundary-layer behaviour accurately. Results from the prediction of the transonic flow over a two-bladed propeller geometry show that the procedure is accurate and efficient for general propeller flow field calculations.

## Introduction

The OPEC oil crisis of the mid 1970s led to a revival in interest in the propeller as a possible fuel-efficient propulsor for aircraft operating at transonic cruise speeds. As a consequence, international research carried out over the last 20 years has led to the development of the advanced propeller concept; a multi bladed, highly loaded, variable pitch, unducted propeller, that can achieve a significantly higher fuel efficiency than an equivalent technology turbofan engine operating at competitive speeds and altitudes. High fuel efficiency is achieved through the use of highly swept and twisted blades that incorporate thin airfoil sections in their outboard regions.

To-date, potential cabin noise problems, the reduction of aviation fuel costs, and the perceived prejudice of the general public towards propeller driven aircraft, have hindered the introduction of advanced propellers on large commercial aircraft.

*Lecturer, Member AIAA



Meanwhile, propellers showing blade shape characteristics clearly influenced by advanced propeller research have been introduced on regional and general aviation aircraft that were traditionally propeller driven. However, some interest still remains in the advanced propeller concept both for commercial and military use, as fuel efficiency will inevitably become of crucial importance in the development of future propulsion systems.

In order to further improve the aerodynamic and acoustic performance of the advanced propeller, it is necessary to fully understand the complex flow patterns occurring on the blade and spinner surfaces and in the general surrounding flow field. To this end, a computational fluid dynamics (*CFD*) procedure has been developed to predict the three-dimensional, compressible, viscous flow field around general propeller configurations with the inflow along the main axis of the propeller. This procedure is tailored towards advanced propeller flow field calculations but is in no way restricted to these geometries. The procedure itself consists of the use of an accurate and efficient flow solver recently developed by the author, coupled with a commercially available turbomachinery grid generator that allows rapid grid generation around propeller geometries.

The flow solver, named NAVPROP, solves the Reynolds-Averaged-Navier-Stokes equations formulated in a steadily-rotating, blade-attached, non-inertial reference frame. With this formulation the flow can then be treated as steady relative to the propeller. To solve the governing equations, a cell-centre finite volume scheme is employed. Explicit multistage Runge-Kutta time stepping marches the solution towards a steady-state, while local time-stepping, implicit residual averaging, and multigrid are employed to increase the rate of convergence. The grid generator, named TIGER, is used to discretise the computational domain into a contiguous set of hexahedral cells as part of a C-H grid system.

The development of NAVPROP has been the focus of this work and is described in detail, while the operation of TIGER is briefly described. Results are presented from three test cases.

## Flow Solver

The governing equations of viscous flow, i.e., the Navier-Stokes equations, are initially formulated using the flow model of a fixed finite control volume in a non-inertial reference frame that is attached to the rotating propeller[1]. A right-handed Cartesian coordinate system is employed and it is assumed that the propeller rotates with constant angular velocity ω around the x axis. The equations thus obtained are then re-written in partial differential equation form, non-dimensionalised using a standard non-dimensionalisation procedure, and finally transformed to a body-fitted curvilinear coordinate system.

Letting ρ, u, v, w, p, and E denote density, the x, y, and z components of the absolute velocity, static pressure and total energy per unit volume respectively, the final form of the governing equations in vector form is as follows

$$\frac{\partial (J^{-1}Q)}{\partial t}+\frac{\partial F}{\partial \xi}+\frac{\partial G}{\partial \eta}+\frac{\partial H}{\partial \zeta}=I+\frac{\partial F_v}{\partial \xi}+\frac{\partial G_v}{\partial \eta}+\frac{\partial H_v}{\partial \zeta} \quad (1)$$

where the vectors are

$$Q=\begin{bmatrix}\rho\\ \rho u\\ \rho v\\ \rho w\\ E\end{bmatrix}$$

$$F=J^{-1}\begin{bmatrix}\rho U\\ \rho uU+\xi_x p\\ \rho vU+\xi_y p\\ \rho wU+\xi_z p\\ (E+p)U-\xi_t p\end{bmatrix}$$

$$G=J^{-1}\begin{bmatrix}\rho V\\ \rho uV+\eta_x p\\ \rho vV+\eta_y p\\ \rho wV+\eta_z p\\ (E+p)V-\eta_t p\end{bmatrix}$$

$$H=J^{-1}\begin{bmatrix}\rho W\\ \rho uW+\zeta_x p\\ \rho vW+\zeta_y p\\ \rho wW+\zeta_z p\\ (E+p)W-\zeta_t p\end{bmatrix}$$

$$I=J^{-1}\begin{bmatrix}0\\ 0\\ \rho\omega w\\ -\rho\omega v\\ 0\end{bmatrix}$$

$$F_v=\frac{\sqrt{\gamma}Ma_\infty J^{-1}}{Re_\infty}\begin{bmatrix}0\\ \xi_x\tau_{xx}+\xi_y\tau_{yx}+\xi_z\tau_{zx}\\ \xi_x\tau_{xy}+\xi_y\tau_{yy}+\xi_z\tau_{zy}\\ \xi_x\tau_{xz}+\xi_y\tau_{yz}+\xi_z\tau_{zz}\\ \xi_x b_x+\xi_y b_y+\xi_z b_z\end{bmatrix} \quad (2)$$

$$G_v=\frac{\sqrt{\gamma}Ma_\infty J^{-1}}{Re_\infty}\begin{bmatrix}0\\ \eta_x\tau_{xx}+\eta_y\tau_{yx}+\eta_z\tau_{zx}\\ \eta_x\tau_{xy}+\eta_y\tau_{yy}+\eta_z\tau_{zy}\\ \eta_x\tau_{xz}+\eta_y\tau_{yz}+\eta_z\tau_{zz}\\ \eta_x b_x+\eta_y b_y+\eta_z b_z\end{bmatrix}$$

$$H_v=\frac{\sqrt{\gamma}Ma_\infty J^{-1}}{Re_\infty}\begin{bmatrix}0\\ \zeta_x\tau_{xx}+\zeta_y\tau_{yx}+\zeta_z\tau_{zx}\\ \zeta_x\tau_{xy}+\zeta_y\tau_{yy}+\zeta_z\tau_{zy}\\ \zeta_x\tau_{xz}+\zeta_y\tau_{yz}+\zeta_z\tau_{zz}\\ \zeta_x b_x+\zeta_y b_y+\zeta_z b_z\end{bmatrix}$$

U, V, and W are the contravariant velocity components in the ξ, η, and ζ directions respectively, and are defined as

$$\begin{aligned}U&=\xi_x u+\xi_y v+\xi_z w+\xi_t\\ V&=\eta_x u+\eta_y v+\eta_z w+\eta_t\\ W&=\zeta_x u+\zeta_y v+\zeta_z w+\zeta_t\end{aligned} \quad (3)$$

and the shear stress terns are

$$\tau_{xx}=\frac{2\mu}{3}\left(2\frac{\partial u}{\partial x}-\frac{\partial v}{\partial y}-\frac{\partial w}{\partial z}\right)$$

$$\tau_{yy}=\frac{2\mu}{3}\left(2\frac{\partial v}{\partial y}-\frac{\partial u}{\partial x}-\frac{\partial w}{\partial z}\right)$$

$$\tau_{zz}=\frac{2\mu}{3}\left(2\frac{\partial w}{\partial z}-\frac{\partial u}{\partial x}-\frac{\partial v}{\partial y}\right)$$

$$\tau_{xy} = \tau_{yx} = \mu\left(\frac{\partial v}{\partial x} + \frac{\partial u}{\partial y}\right)$$
$$\tau_{xz} = \tau_{zx} = \mu\left(\frac{\partial u}{\partial z} + \frac{\partial w}{\partial x}\right) \qquad (4)$$
$$\tau_{yz} = \tau_{zy} = \mu\left(\frac{\partial v}{\partial z} + \frac{\partial w}{\partial y}\right)$$

$$b_x = u\tau_{xx} + v\tau_{xy} + w\tau_{xz} + k\frac{\partial T}{\partial x}$$
$$b_y = u\tau_{yx} + v\tau_{yy} + w\tau_{yz} + k\frac{\partial T}{\partial y}$$
$$b_z = u\tau_{zx} + v\tau_{zy} + w\tau_{zz} + k\frac{\partial T}{\partial z}$$

In the equations given above $\xi_x$, $\xi_y$, $\xi_z$, $\xi_t$, $\eta_x$, $\eta_y$, $\eta_z$, $\eta_t$, $\zeta_x$, $\zeta_y$, $\zeta_z$, and $\zeta_t$ are the metrics of the transformation, and $J^{-1}$ is the Jacobian of the inverse transformation.

Additionally, $\mu$ and k are the molecular or laminar coefficients of viscosity and thermal conductivity respectively, $\gamma$ is the ratio of specific heats, $Ma_\infty$ is the freestream Mach number, and $Re_\infty$ is the freestream Reynolds number. Stokes' hypothesis was employed in the writing of the shear stress terms in order to relate the first (laminar) and the second coefficients of viscosity.

The above set of unsteady equations can be solved for laminar flow problems but not for turbulent flows ones because of the very small spatial and temporal scales required and the computational resources this entails. In order to obtain meaningful results for turbulent flow problems, a time-averaged form of these equations is solved. The time-averaged equations, called the Reynolds-Averaged Navier-Stokes equations, have the same form as the original ones presented, except that extra terms such as apparent stresses and heat flux terms appear. Closure for this system of equations is achieved by using an eddy viscosity hypothesis, which assumes that these extra terms can be related to the gradients of mean flow variables. To this end, the laminar viscosity in the original equations is replaced by an effective viscosity defined as

$$\mu_e = \mu_l + \mu_t \qquad (5)$$

where $\mu_e$ is the effective viscosity, $\mu_l$ is the laminar viscosity, and $\mu_t$ is the turbulent eddy viscosity. Also, the thermal conductivity is replaced by the following using a constant Prandlt number assumption

$$k_e = \frac{\gamma}{\gamma - 1}\left[\left(\frac{\mu}{Pr}\right)_l + \left(\frac{\mu}{Pr}\right)_t\right] \qquad (6)$$

where again l and t denote laminar and turbulent respectively, and Pr is the Prandtl number. The laminar and turbulent Prandlt numbers are taken to be 0.72 and 0.9 respectively in this work. The eddy viscosity is computed using the algebraic two-layer eddy-viscosity model of Baldwin and Lomax[2], and once known the effective thermal conductivity can be calculated.

It is worth noting that with this particular formulation of the governing equations the flow around a steadily rotating propeller with an inflow at zero angles of incidence and yaw can be treated as steady and results in an algorithm that is far more efficient than one that solves for the unsteady flow field in an inertial reference frame.

## Solution Procedure

As mentioned earlier the computational domain is discretised into a contiguous set of structured hexahedral cells as part of a C-H grid system and Equation 1 is integrated over each cell in the domain. A cell-centre finite-volume scheme is employed in the solver, with the cell centre values of the conserved variables representing cell average quantities. At the cell faces central differencing is used for the evaluation of the convective fluxes, while the viscous fluxes are easily evaluated once the values of the velocity and temperature derivatives are known at these locations. These derivatives require careful evaluation and are calculated using the method described by Lacor et al[3].

A controlled amount of artificial dissipation is added to the resulting equations in order to prevent odd-even point decoupling associated with a central-difference scheme and the appearance of undesirable oscillations near shock waves and stagnation points. The artificial dissipation model used is basically the one originally introduced by Jameson, Schmidt, and Turkel[4], and consists of blended first and third differences of the conserved variables for each equation. Anisotropic scaling of the dissipation terms is employed to prevent the addition of excessive dissipation in the high aspect ratio cells that are necessary when performing viscous flow calculations. Two different scaling models, by Martinelli[5] and Radespiel[6], are used and have proven satisfactory.

Following the spatial discretisation, a system of ordinary differential equations is obtained. To integrate these equations in time to a steady-state an explicit, multistage, Runge-Kutta time-stepping scheme is used. A five-stage scheme is chosen with the artificial dissipation terms being evaluated on the first, third, and fifth stages only, and frozen on the second and fourth. This scheme has good high frequency damping properties, which is important if it is to drive the multigrid scheme described below.

To significantly increase the rate of convergence to a steady state, three well-proven convergence acceleration techniques associated with explicit type schemes are employed concurrently: local time-stepping, implicit residual averaging, and multigrid. With local time-stepping each cell in the computational domain is advanced in time using its own time-step that is determined by stability considerations. The time accuracy of the solution is destroyed but a significant increase in convergence rate is achieved. Implicit residual averaging is used to both extend the stability range and robustness of the basic time-stepping scheme. The residual smoothing is applied in factored form. A Full approximation storage (FAS) multigrid scheme based on the work of Jameson[7] is employed. For the multigrid process, coarser grids are obtained by deleting every other mesh line in each coordinate direction of the next finer grid. The solution and residuals are transferred to the coarser grid and a forcing function constructed so that the coarse grid solution is driven by the residuals collected from the next finer grid. Corrections are transferred between grid levels using trilinear interpolation. The work split between by the various grid levels is achieved using a fixed cycling strategy. Two alternatives are implemented in the solver: a V-cycle and a W-cycle. The robustness of the multigrid scheme is significantly enhanced by the smoothing of the coarse grid corrections before addition to the fine grid solution. This reduces high-frequency oscillations introduced by the trilinear interpolation. The factored scheme used for the residual averaging, but with constant coefficients, appear to be the most efficient way of achieving this.

The flow around a propeller with the inflow at zero angles of incidence and yaw is periodic in the circumferential direction from one inter-blade region to the next. It is therefore necessary to solve for the flow in one inter-blade region only. A C-H type mesh is used to discretise the computational domain, with the C-part in the axial direction and the H-part in the circumferential direction. The boundary conditions are implemented using an extra layer of ghost cells exterior to the flow domain and are described in detail by Boyle[8-10].

A Full Multigrid Method (FMG) is used to provide a well-conditioned starting solution for the finest mesh. With the FMG strategy, the solution is initialised on the coarsest of a specified series of grids and iterated for a set number of multigrid cycles using the FAS multigrid scheme. The solution is then transferred to the next finer grid using trilinear interpolation. This process is repeated until the finest mesh level is reached. In the present scheme two or three FMG levels are used and a maximum of three multigrid levels used on all grid levels. 50-100 multigird cycles are typically performed on each grid level. The freestream values of the variables are used as the starting solution on the coarsest grid.

## Grid Generator

The generation of well-defined grids for propeller configurations can be a difficult and time-consuming task because of the complexity of the geometries involved. This is especially true for viscous flow field calculations where mesh resolution is of particular importance for accurate results. In the past the generation of grids has been a bottleneck in propeller CFD analyses, but fortunately this is no so today due to availability of high performance grid generators. The grids employed in this work were generated using TIGER[11,12] (Turbomachinery Interactive Grid Generation), Version X3.1, a commercially available grid generator tailored specifically towards turbomachinery applications that allows grids to be generated rapidly and with relative ease. Using TIGER, a structured C-H grid system is used to discretise the computational domain as discussed above, with the C and H-type grids in the streamwise and the circumferential directions respectively. To demonstrate the use of TIGER a C-H grid is generated for the two bladed NACA 10-(3)(066)-033 propeller shown in Figure 1. Sections from a low-density mesh for this configuration are shown in Figures 2 to 4. The grid clustering near the blade leading and trailing edges and near the blade root and tip can be clearly seen.

## Results

### Introduction

As an effective starting point in the validation of the accuracy of NAVPROP, results were

obtained for two often employed test cases. The two cases were for incompressible laminar and turbulent flow over a smooth flat plate. These test cases were employed as calculated data can be compared directly with theory.

To demonstrate the operation of the overall procedure, results are also presented for the case of inviscid transonic flow over a two-bladed NACA 10-(3)(066)-033 propeller. This test case was selected to enable comparison of predictions with reliable wind tunnel measurements.

**Case 1: Laminar Flow Over a Smooth Flat Plate**

The first set of results that is presented is for the case of incompressible laminar flow over a smooth flat plate with zero freestream pressure gradient in the axial direction. In order to approximate incompressible flow the freestream Mach number was set at 0.3. The Reynolds number based on plate length was $Re_L$=1,000,000. This high value was employed to ensure that the calculated boundary layer thickness was small in comparison to the length of the computational domain in the direction normal to the plate, i.e., the vertical direction. The computational domain had non-dimensional lengths of 1.0, 0.1, and 0.l in the axial, vertical, and transverse directions respectively. The grid dimensions were 97x65x9 in the axial, vertical, and transverse directions also. Note that only 9 cells were required in the transverse direction as there should be no tranverse variations of the flow variables.

The variation of the skin friction coefficient with axial location is shown in Figure 5, while axial velocity profiles at various axial locations along the plate are presented in Figure 6. In both figures the predictions are compared with the exact solutions of Blasius[13]. The velocity profiles all collapse onto a single curve that compares very well with the Blasius curve. Overall the comparisons are very good. Velocity vectors in the boundary layer at an axial location near the plate trailing edge are shown in Figure 7.

**Case 2: Turbulent Flow Over a Smooth Flat Plate**

The second test case was for incompressible turbulent flow over a smooth flat plate with zero freestream pressure gradient. A computational domain with the same dimensions and grid density as employed for the first test case were used for this case also, but with higher grid spacing the vertical direction in order to accurately resolve the laminar wall-layer region. The chosen Reynolds number was $Re_L$=10,000,000. The results are presented in Figure 8 to 10. Figure 8 shows the calculated and theoretical variation of skin friction coefficient with axial position The two curves differ slightly but show the same variation with axial position. Similar trends in skin friction were also observed by other researchers[14]. Axial velocity profiles at several axial locations are shown in Figure 9. The laminar wall layer, the overlap layer, and the turbulent outer layer are all distinctly captured in each profile. The theoretical law of the wall and logarithmic-overlap layer law are also plotted and compare very well with the predictions. As with the previous test case velocity vectors in the boundary layer near the plate trailing edge are presented in Figure 10.

**Case 3: Inviscid Transonic Flow Around the NACA 10-(3)(066)-033 Propeller**

The two-bladed NACA 10-(3)(066)-033 propeller[15] is composed of NACA 16 series airfoil sections and has a rectangular planform. A series of wind tunnel tests were carried out by NACA around 1950 on full-scale propellers, including a 10-ft diameter NACA 10-(3)(066)-033 propeller to determine blade section characteristics by measuring the pressure distributions on the airfoil sections under operating conditions. The measurements for the NACA 10-(3)(066)-033 propeller are extensive and it is a standard test case for validating a propeller algorithm. For this test case NAVPROP was run in inviscid mode. A freestream Mach number and advance ratio of 0.56 and 0.23 were chosen respectively. The blade angle at 75% radius was 45°. A medium density grid with 129x49x73 points in the axial, radial, and circumferential directions respectively was used. The results of the test case are presented in Figure 11 to 14. The convergence history and the development of the thrust coefficient $C_T$ are shown in Figures 11 and 12 respectively. For this test case four FMG levels were specified and the solver was allowed to converge to machine zero on each level. This was done for demonstration purposes only. Convergence was rapid with engineering accuracy (i.e., four orders reduction in the residual of the continuity equation) achieved in 138 multigrid cycles and machine zero (i.e., thirteen orders reduction) in 707 cycles on the finest grid level. A comparison of computed and measured surface pressure coefficient at four radial locations is shown in Figure 13. Note that the computed pressures were obtained at the experimental locations using simple interpolation. The comparison between the predictions and measurements is very good considering the complexity of the flow field. A

shock wave can be clearly identified on the suction surface and spans from about 65% of the blade radius out to the blade tip. The disparity in surface pressure can be attributed to the omission of viscous effects and to the fact that the blade deformation due to centrifugal and aerodynamic loading was not accounted for. The undeformed blade shape, also called the "cold blade" shape, was used in the present calculation. Contours of relative Mach number at the cell centres adjacent to the blade pressure and suction surfaces are shown in Figure 14. The supersonic flow region and the shock wave on the suction surface can be clearly identified in the figure.

## Concluding Remarks

An efficient procedure has been developed to predict the viscous flow around general propeller geometries under zero angle of incidence and zero angle of yaw inflow conditions. The procedure consists of a recently developed viscous flow solver and a commercially available turbomachinery grid generator. Initial validation of the procedure has demonstrated its ability to accurately and efficiently predict transonic propeller flow fields, and the ability of the flow solver to accurately capture laminar and turbulent boundary layer behaviour. Further validation is already underway and results of viscous test cases will be presented in the very near future.

## Acknowledgements

This work was partially funded by the Dublin Institute of Technology under the Seed Research Funding Programme and is the result of two years of effort. The author would like to thank the School of Engineering for supporting this research and also Prof. Eli Turkel from Tel Aviv University for his continued help and advice.

## References

[1] Holmes, D. G., and Tong, S. S., "*A Three-Dimensional Euler Solver for Turbomachinery Blade Rows*", Journal of Engineering for Gas Turbines and Power, Vol. 107, pp. 258-264, 1985.

[2] Baldwin, B. S., and Lomax, H., "*Thin Layer Approximation and Algebraic Model for Separated Flows*", AIAA Paper No. 78-257, 1978.

[3] Lacor, C., Hirsch, C., Leonard, B., and Lessani, B., *"A 3D Navier-Stokes Solver Using Unstructured, Hexahedral Meshes With Adaption"*, AIAA Paper No. 99-3364, 1999.

[4] Jameson, A., Schmidt, W., and Turkel, E., "*Numerical Solutions of the Euler Equations by Finite Volume Methods Using Runge-Kutta Time-Stepping Schemes*", AIAA Paper No. 81-1259, 1981.

[5] Martinelli, L., "*Calculation of Viscous Flows Using a Multigrid Method*", Ph.D. Thesis, Department of Mechanical and Aerospace Engineering, Princeton University, Princeton, New Jersey, USA, 1987.

[6] Radespiel, R., Rossow, C., and Swanson, R. C., *"Efficient Cell-Vertex Multigrid Scheme for Three-Dimensional Navier-Stokes Equations"*, AIAA Journal, Vol. 28, No. 8, pp. 1464-1472, 1990.

[7] Jameson, A., *"Multigrid Algorithms for Compressible Flow Calculations"*, MAE Report 1743, Princeton University, Princeton, New Jersey, USA, Text of lecture given at the 2nd European Conference on Multigrid Methods, Cologne, Germany, 1985.

[8] Boyle, F. J., "*Development of CFD Algorithms for Transient and Steady Aerodynamics*", Ph.D. Thesis, Department of Mechanical Engineering, National University of Ireland, Galway, Ireland, 1999.

[9] Boyle, F. J., O'Flaherty, M. P., and Eaton, J. A., "*Validation of Efficient Euler Algorithms for Advanced Propellers Under Transonic and Subsonic Conditions*", AIAA Paper No. 99-3228, 1999.

[10] Boyle, F. J., O'Flaherty, M. P., and Eaton, J. A., "*Three-Dimensional Euler Solutions for Axisymmetric and Non-Axisymmetric Advanced Propeller Flows*", AIAA Paper No. 99-2386, 1999.

[11] Shih, A., TIGER User Guide: Version X3.1, Catalpa Research Incorporated, Champaign, Illinois, USA, 2000.

[12] Shih, M. H., Soni, B. K., Yu, T. Y., and Shaunak, S., "*TIGER: A Turbomachinery Grid Generation/Simulation System*", AIAA Paper No. 94-0207, 1994.

[13] White, F. M, Fluid Mechanics, McGraw-Hill Book Company, 4th Edition, 1999.

[14] Liu, F., and Jameson, A., *"Multigrid Navier-Stokes Calculations for Three-Dimensional Cascades"*, AIAA Journal, Vol. 31, No. 10, 1993.

[15] Maynard, J. D., and Murphy, M. P., "*Pressure Distributions on the Blade Sections of the NACA 10-(3)(066)-033 Propeller Under Operating Conditions*", NACA Research Memorandum L9L12, 1950.

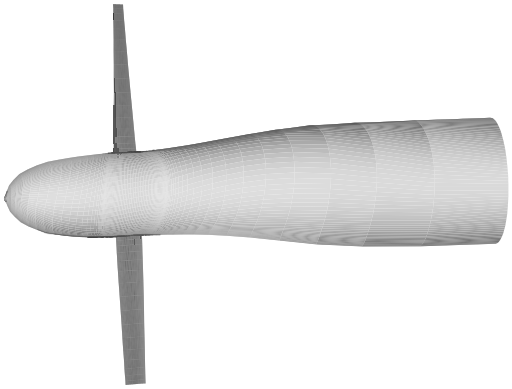

***Figure 1.*** The two-bladed NACA 10-(3)(066)-033 propeller.

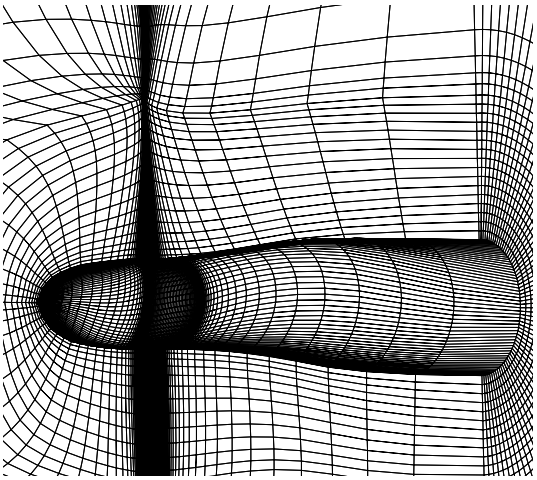

***Figure 3.*** A section of the C-H grid around the two-bladed NACA 10-(3)(066)-033 propeller.

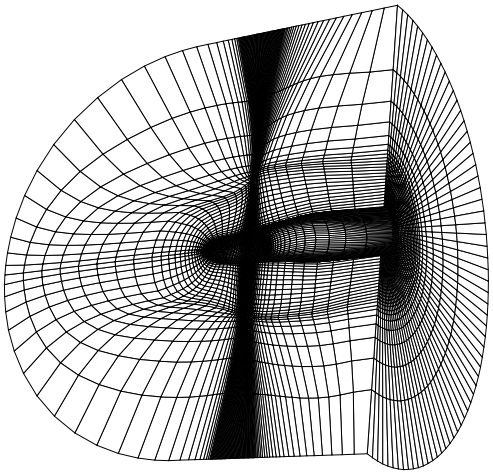

***Figure 2.*** The computational domain for the NACA 10-(3)(066)-033 propeller flow field calculation.

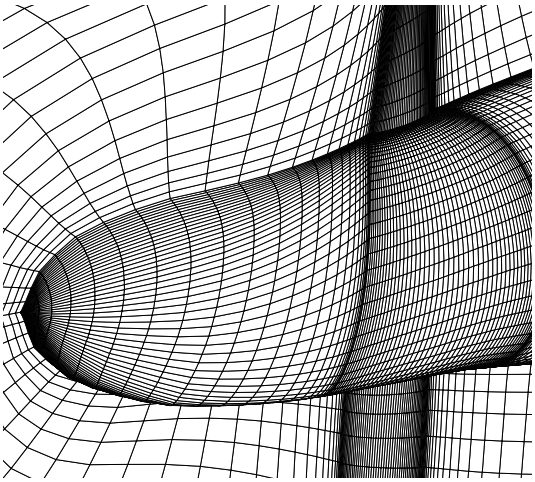

***Figure 4.*** A close-up view of the inner part of the grid around the NACA 10-(3)(066)-033 propeller.

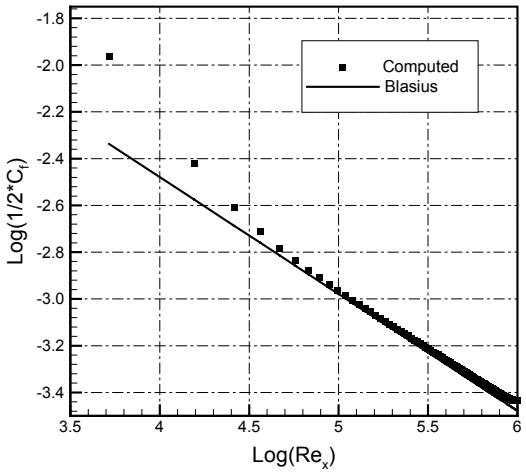


***Figure 5.*** Comparison of predicted skin friction coefficient with Blasius theoretical solution for laminar flow over a flat plate.

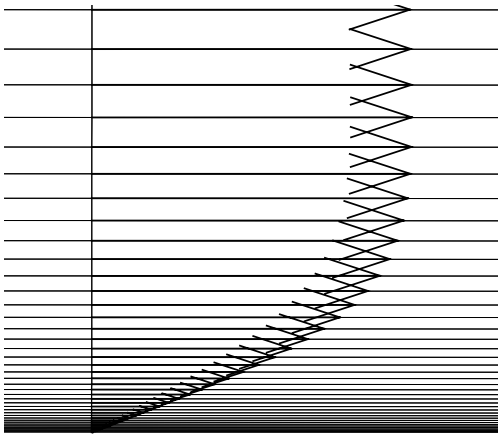

***Figure 7.*** Axial velocity vectors in the laminar boundary layer at an axial location near the plate trailing edge.

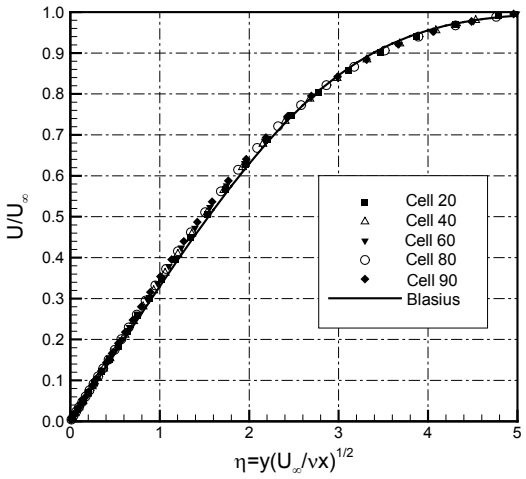


***Figure 6.*** Comparison of predicted axial velocity profiles with Blasius theoretical profile for laminar flow over a flat plate.

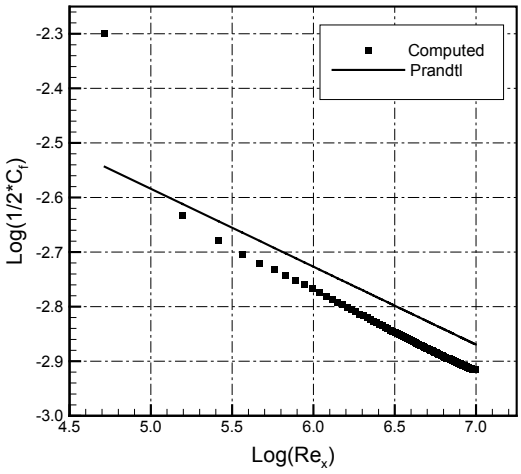


***Figure 8.*** Comparison of predicted skin friction coefficient with Prandtl theoretical solution for turbulent flow over a flat plate.

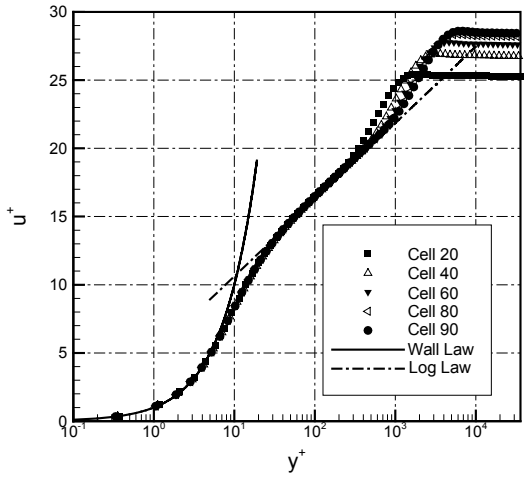


***Figure 9.*** Comparison of predicted axial velocity profiles with theoretical laws for turbulent flow over a flat plate.

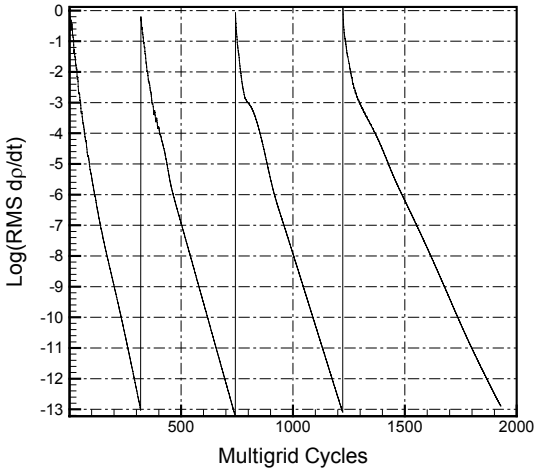


***Figure 11.*** Convergence history of the NACA 10-(3)(066)-033 propeller flow field calculation. $Ma_\infty$=0.56, J=2.3, and $\beta_{3/4}$=45˚.

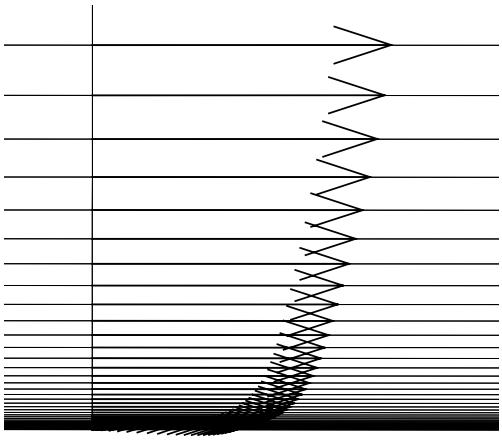

***Figure 10.*** Axial velocity vectors in the turbulent boundary layer at an axial location near the plate trailing edge.

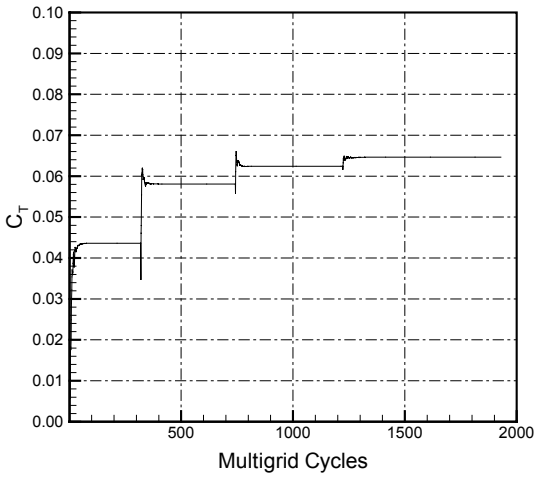


***Figure 12.*** Development of the thrust coefficient $C_T$ during the NACA 10-(3)(066)-033 propeller flow field calculation. $Ma_\infty$=0.56, J=2.3, and $\beta_{3/4}$=45˚.

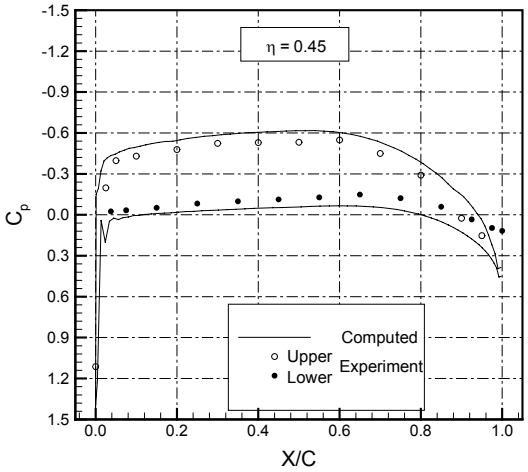


***Figure 13a.*** Comparison of chordwise variation of computed and measured surface pressure for the NACA 10-(3)(066)-033 propeller at a radial location of 0.45. $Ma_\infty$=0.56, J=2.3, and $\beta_{3/4}$=45˚.

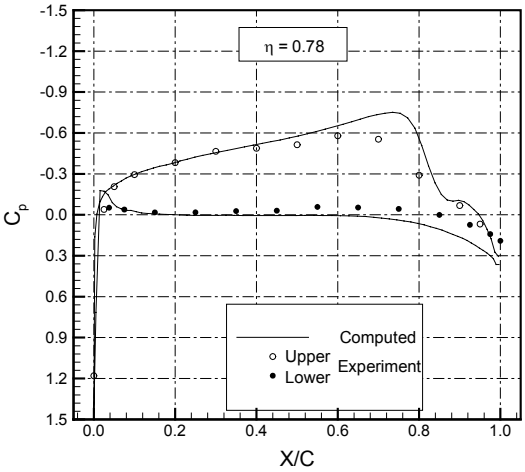


***Figure 13c.*** Comparison of chordwise variation of computed and measured surface pressure for the NACA 10-(3)(066)-033 propeller at a radial location of 0.78. $Ma_\infty$=0.56, J=2.3, and $\beta_{3/4}$=45˚.

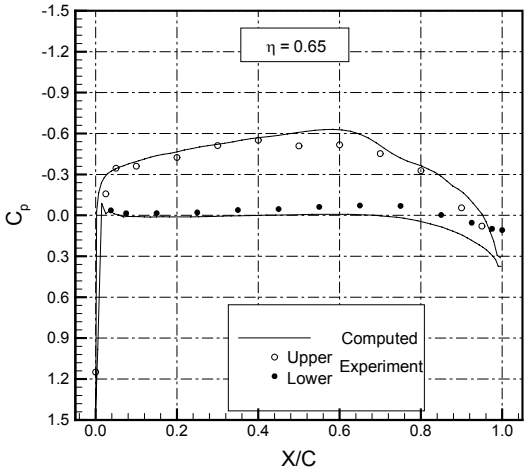


***Figure 13b.*** Comparison of chordwise variation of computed and measured surface pressure for the NACA 10-(3)(066)-033 propeller at a radial location of 0.65. $Ma_\infty$=0.56, J=2.3, and $\beta_{3/4}$=45˚.

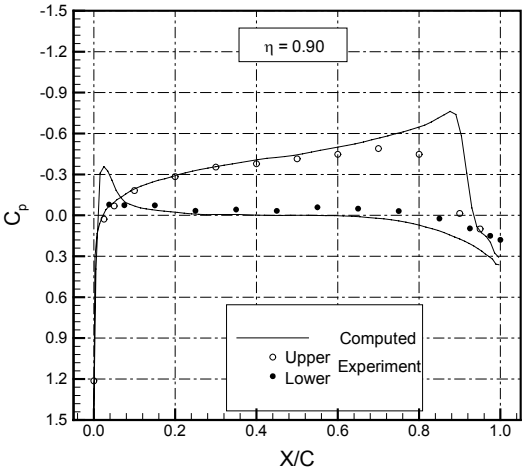


***Figure 13d.*** Comparison of chordwise variation of computed and measured surface pressure for the NACA 10-(3)(066)-033 propeller at a radial location of 0.90. $Ma_\infty$=0.56, J=2.3, and $\beta_{3/4}$=45˚.

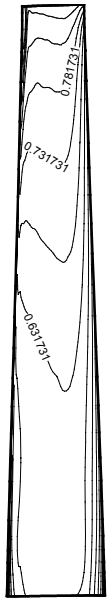


***Figure 14a.*** Contours of relative Mach number at the cell centres adjacent to the pressure surface of the NACA 10-(3)(066)-033 propeller blade. $Ma_\infty$=0.56, J=2.3, $\beta_{3/4}$=45˚, and $\Delta Ma_{rel}$=0.05.

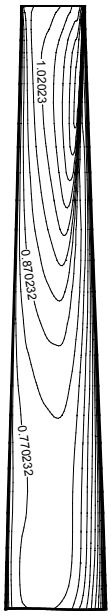


***Figure 14b.*** Contours of relative Mach number at the cell centres adjacent to the suction surface of the NACA 10-(3)(066)-033 propeller blade. $Ma_\infty$=0.56, J=2.3, $\beta_{3/4}$=45˚, and $\Delta Ma_{rel}$=0.05.